

# ACCEPTED VERSION

Elliott W. Lewis, Timothy C.W. Laua, Zhiwei Suna, Zeyad T. Alwahabi, Graham J. Nathan  
**The effect of particle size and volumetric loading on the gas temperature distributions in a particle-laden flow heated with high-flux radiation**  
International Journal of Heat and Mass Transfer, 2022; 182:122041-1-122041-13

© 2021 Elsevier Ltd. All rights reserved.

This manuscript version is made available under the CC-BY-NC-ND 4.0 license  
<http://creativecommons.org/licenses/by-nc-nd/4.0/>

Final publication at: <http://dx.doi.org/10.1016/j.ijheatmasstransfer.2021.122041>

## PERMISSIONS

<https://www.elsevier.com/about/policies/sharing>

Accepted Manuscript

Authors can share their [accepted manuscript](#):

24 Month Embargo

### After the embargo period

- via non-commercial hosting platforms such as their institutional repository
- via commercial sites with which Elsevier has an agreement

In all cases [accepted manuscripts](#) should:

- link to the formal publication via its DOI
- bear a CC-BY-NC-ND license – this is easy to do
- if aggregated with other manuscripts, for example in a repository or other site, be shared in alignment with our [hosting policy](#)
- not be added to or enhanced in any way to appear more like, or to substitute for, the published journal article

**28 March 2024**

<http://hdl.handle.net/2440/134915>

# The effect of particle size and volumetric loading on the gas temperature distributions in a particle-laden flow heated with high-flux radiation

Elliott W. Lewis<sup>1,3</sup>, Timothy C. W. Lau<sup>1,3,4</sup>, Zhiwei Sun<sup>1,3</sup>,  
Zeyad T. Alwahabi<sup>2,3</sup>, and Graham J. Nathan<sup>1,3</sup>

<sup>1</sup>*School of Mechanical Engineering, University of Adelaide, Australia*

<sup>2</sup>*School of Chemical Engineering and Advanced Materials, University of Adelaide, Australia*

<sup>3</sup>*Centre for Energy Technology, University of Adelaide, Australia*

<sup>4</sup>*UniSA STEM, University of South Australia, Australia*

## Abstract

The instantaneous, spatially resolved gas-phase temperature distribution within a particle-laden flow heated using high-flux radiation has been measured for a series of heating fluxes, particle volumetric loadings and particle diameters using two-colour laser induced fluorescence of toluene. The temperature of the gas downstream from the start of the heating region was found to increase with an increase in heat flux, an increase in particle loading and a decrease in particle diameter. Coherent regions of high and low temperature in the instantaneous flow associated with spatial variations in the particle distribution were identified for all particle diameters investigated. The time-averaged gas-phase temperature on the jet axis was found to increase approximately linearly with distance in the region downstream from the heating beam to the edge of the measurement region investigated, indicating near-constant convective heat transfer due to the large temperature difference between the gas and radiatively heated particles throughout this region. The axial gradient of gas-phase temperature with distance was also calculated using a simplified, one-dimensional heat transfer model. The difference between the model and measurements was, on average, less than 20%, with the magnitude of this difference found

to increase with a decrease in particle diameter and an increase in particle loading.

## 1 Introduction

Non-isothermal, high temperature particle-laden flows with strong radiative heat transfer remain poorly understood despite being widely utilised in industrial processes, such as the calcination of alumina in fluid-flash calciners (Fish 2016) and the decomposition of calcium carbonate in kilns (Oates 1998). These processes often require temperatures in excess of 1000 °C for efficient operation, with the flow historically heated by the combustion of fossil fuels. Low-carbon energy sources that have been identified as potential alternatives include hydrogen, electricity and concentrated sunlight (Energy Transitions Commission 2020), with particle-based concentrated solar thermal (CST) receivers showing great potential for long-term operation at the required temperatures (Ho 2016). Laboratory-scale CST receivers have also been demonstrated to be functional and technically feasible for the processing of a range of minerals (Steinfeld et al. 1992; Meier et al. 2006; Davis et al. 2017). However, there is currently a lack of understanding of the heat transfer processes and particle-fluid interactions within these particle-laden flows. This hinders the rate of development of both new mineral processing and particle-based solar technologies. Therefore, systematic measurements of the key controlling parameters within these systems are required to optimise efficiencies and lower the risk of uptake for industrial applications.

Both the volumetric distributions of particles and the flow fields of both phases within a particle-laden flow are determined by complex and non-linear phenomena such as turbulence, particle clustering (whereby particles preferentially concentrate in highly localised regions of the flow (Longmire and Eaton 1992; Lau et al. 2019)) and particle-fluid coupling (Balachandar and Eaton 2010). In systems employing heated particles, these phenomena are further complicated by the significant density gradients and buoyancy-induced motions generated from thermal gradients in the gas-phase (Frankel et al. 2016). The resultant heat transfer in the system is coupled to the fluid motions through the mutually interacting processes of particle-fluid momentum transport, convection and buoyancy (Zamansky et al. 2014). Additionally, the radiation absorbed by individual particles, and the subsequent particle temperature change, is highly non-uniform throughout the flow due to attenuation and multiple scattering of the incident radiation (Kumar et al. 2018). This non-uniform radiation absorption is particularly significant for the densely seeded flows typically used in industrial processes, in which

particle volumetric loadings of  $\phi > 10^{-3}$  are common, where  $\phi = \dot{V}_p/\dot{V}_f$  is the ratio of the volumetric flow rate of the particles to that of the fluid. Furthermore, in radiatively heated particle-laden channel flows, particle clustering has been shown to lead to spatially and temporally non-uniform gas-phase temperatures (Pouransari and Mani 2016; Banko et al. 2020). The combination of these complex, mutually interacting phenomena lead to significant challenges in modelling the system without resorting to computationally cost-prohibitive direct numerical simulations. Therefore, in-situ and well-resolved experimental measurements are required to provide both the insights into the heat transfer processes in particle based receivers and the datasets needed for the development and validation of numerical models.

The diameter and volumetric loading of particles are two key parameters that significantly affect the particle-fluid interactions and heat transfer in particle-laden flows. Previous simulations of particle-based CST receivers have shown that both the solar receiver efficiency, defined as the proportion of the total solar heat entering the system that is absorbed by particles, and the average particle temperature at the outlet, decrease with an increase in particle diameter (Miller and Koenigsdorff 1991; Chen et al. 2006). The solar receiver efficiency was also found to increase with particle volumetric loading, because a greater proportion of the incident radiation is absorbed by the particles (Siegel et al. 2010). Conversely, the average particle temperature at the outlet decreases with increasing loading because individual particles are increasingly likely to be in the shadow of those closer to the radiative source. However, these results are limited to spatially averaged data or point-wise measurements, which are unable to resolve the instantaneous gradients in the flow. As such, in-situ, spatially resolved measurements are required to further improve the understanding of heat transfer in these systems. Planar measurements of the temperature in particle-laden flows with strong thermal gradients generated by high-flux radiation are currently available for both the particle-phase (Kueh et al. 2017) and gas-phase (Lewis et al. 2021). The current work extends these measurements by experimentally investigating the effect of particle diameter and volumetric loading on the spatial distribution of the gas-phase temperature in a radiatively heated particle-laden flow.

Laser based techniques are well suited to the measurement of the instantaneous conditions of various parameters in the flow because they can provide planar, spatially resolved data with nanosecond scale temporal resolutions. The technique of LIF, in which the fluorescence emissions from a vapour seeded in trace quantities into the flow are measured, has been used to determine the gas-phase temperature under conditions with strong optical interference, such as in optical engines (Tea et al. 2011), flows with droplets (Jainski et al. 2014) and particle-laden flows (Lewis et al. 2020).

The advantage of LIF for measurements in particle-laden flows over other planar techniques, such as Rayleigh scattering, is that the fluorescence is emitted at longer wavelengths than the excitation laser due to Stokes shift, allowing the separation of the fluorescence signal and elastically scattered light using optical filtering. One method commonly used to determine the temperature from the fluorescence emissions is two-colour LIF, which utilises the red-shift of the fluorescence tracer emission spectrum with temperature. This is done by calculating the ratio of the fluorescence intensity measured in two separate wavelength ranges (Luong et al. 2006). This technique has already been demonstrated to be suitable for gas temperature measurements in particle-laden flows with volumetric loadings of up to  $\phi \approx 10^{-3}$  (Lewis et al. 2020), and for planar measurements in flows heated using high-flux radiation (Lewis et al. 2021). Importantly, the advantage of using the two-colour ratio is that it corrects for the spatial non-uniformity of the signal intensity that can arise in particle-laden flows due to attenuation of the excitation beam and the mixing of tracers with unseeded, ambient fluid. Furthermore, the experimental arrangement for two-colour LIF is relatively simple, employing a single excitation laser and two detection channels. This technique is therefore highly suitable for systematic measurements of the gas-phase temperature distributions in radiatively heated particle-laden flows.

The aim of this paper is therefore to improve the understanding of heat transfer in particle-laden flows heated with high-flux radiation, utilising two-colour LIF thermometry for spatially resolved, planar measurements of the gas-phase temperature. More specifically, the present investigation aims to determine the effect of particle size and volumetric loading on the gas-phase temperature distributions in a flow with well-defined conditions.

## 2 Methodology

### 2.1 Experimental arrangement

Simultaneous measurements of the gas-phase temperature and particle number density, using two-colour LIF and Mie scattering, respectively, were performed in a radiatively heated particle-laden jet arranged as shown in Figure 1. The particle-laden flow issued from a long straight pipe of diameter  $D = 12.6\text{mm}$  with a length-to-diameter ratio of  $L/D = 165$ , which is sufficiently long for the particle-laden flow to approach the fully developed condition (Lau and Nathan 2014). A co-annular pipe of diameter 69 mm was used to generate a well-defined co-flow. Each pipe was centrally aligned within a  $300 \times 300$  mm wind tunnel oriented with the flow direction vertically downwards. The

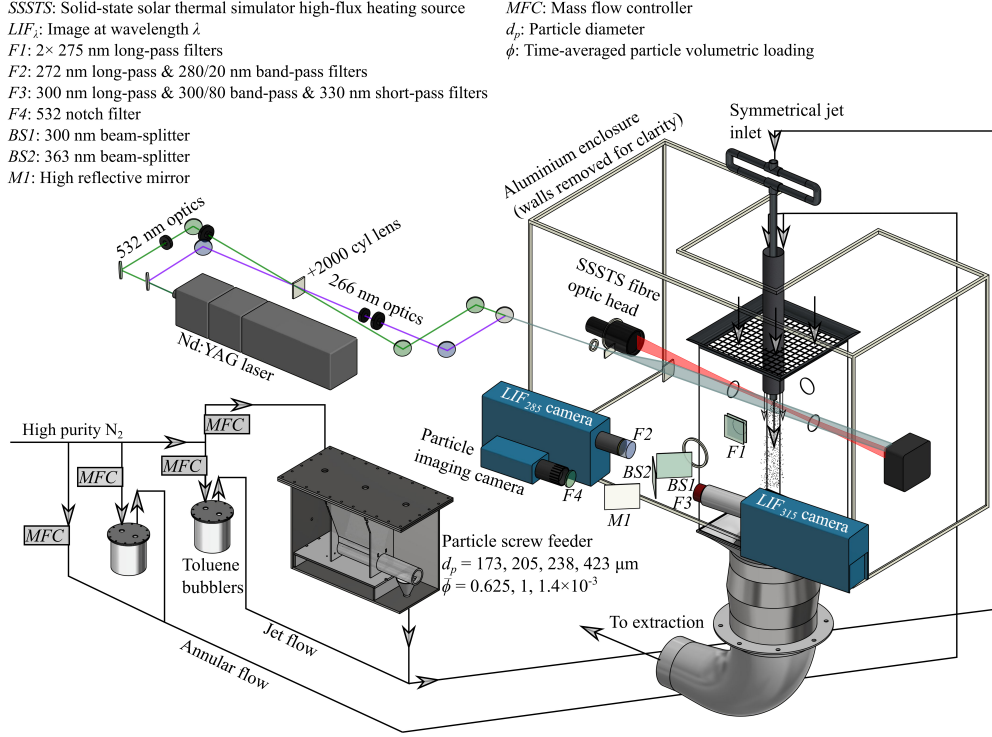


Figure 1: Experimental arrangement for simultaneous two-colour LIF thermometry and particle number density measurements in a flow heated using high-flux radiation.

central jet employed nitrogen with a volumetric flow rate of 25 SLPM. The resultant jet exit Reynolds number was  $Re_D = (\rho_f U_b D) / \mu_f = 3000$ , where  $\rho_f$  and  $\mu_f$  are the fluid density and dynamic viscosity, respectively, and  $U_b = 3.6$  m/s is the gas-phase bulk mean velocity of the jet flow. This flow rate was chosen to maximise the particle residence time in the heating region while remaining sufficiently high to effectively carry the particles. The co-annular flow of 55 SLPM, also of nitrogen, had a bulk mean velocity at the pipe exit of 0.3 m/s. The velocity of the ambient air drawn through the wind tunnel was set to match that of the annular flow to within 20%.

Toluene was chosen as the tracer for two-colour LIF because it is a well characterised species with a relatively strong fluorescence emission that is sensitive to temperature in the range of 290–450 K that is expected for the present investigation (Koban et al. 2004; Faust et al. 2014). Both the central jet and annular flow were seeded with toluene vapour to ensure a strong signal throughout the measurement region, with high purity nitrogen used as the carrier gas to prevent quenching of the toluene fluorescence by molecular

Table 1: Summary of experimental parameters.

Parameter	Symbol	Value
Median particle diameter	$\bar{d}_p$ ( $\mu\text{m}$ )	173, 205, 238, 423
Jet exit Reynolds number	$Re_D$	3000
Jet exit Stokes number	$Sk_D$	86, 121, 163, 514
Mean particle volumetric loading	$\bar{\phi}$ ( $\times 10^{-3}$ )	0.625, 1, 1.4
Heating laser power	$\dot{Q}_0$ (W)	$\bar{\phi} = 1.4 \times 10^{-3}$ 0, 910, 1430, 1950, 2410, 2840
		$\bar{\phi} = 0.625, 1 \times 10^{-3}$ 0, 2840

oxygen (Koban et al. 2005). The toluene vapour was seeded in each flow by bubbling the nitrogen through a separate bath of liquid toluene held at room temperature. The jet flow and co-annular flows were seeded with toluene at concentrations of approximately 0.75% and 0.25% by volume, respectively, with the concentration chosen to differ in these flows to allow a clear identification of the edges of the jet. Particles were introduced to the jet flow at a series of time-averaged volumetric loadings of  $\bar{\phi} = 6.25 \times 10^{-4}$ ,  $1 \times 10^{-3}$  and  $1.4 \times 10^{-3}$ , with a screw feeder located in a sealed enclosure used to control the of particle flow rate. Four distributions of Aluminosilicate ceramic particles (Carbobeat CP) were used, with median diameters  $\bar{d}_p = 173, 205, 238$  and  $423 \mu\text{m}$  each of average sphericity 0.9. Each of the particle diameter distributions were measured using a Malvern Mastersizer 2000, with the results presented in Figure 2. The Stokes number of the median diameter for each particle case, evaluated at the jet exit for the large eddy time scale, was  $Sk_D = (\rho_p \bar{d}_p^2 U_b) / (18 \mu_f D) = 86, 121, 263$  and  $514$ , respectively, where  $\rho_p = 3270 \text{ kg/m}^3$  is the density of the particles. A summary of these experimental parameters is presented in Table 1.

The second and fourth harmonic outputs from a single Nd:YAG laser (Quantel Q-smart), with respective wavelengths of 532 (to image scattering from particles) and 266 nm (to generate toluene fluorescence), were each formed into vertical co-planar sheets. Each sheet had an approximate height and thickness of 60 and 0.6 mm, respectively, and was aligned with the central axis of the pipe with the top edge of the sheet 3 mm from the jet exit plane. The laser pulse frequency was 10 Hz with pulse energies of 0.5 and 18 mJ/pulse for the 532 nm and 266 nm sheets, respectively. The radiat-

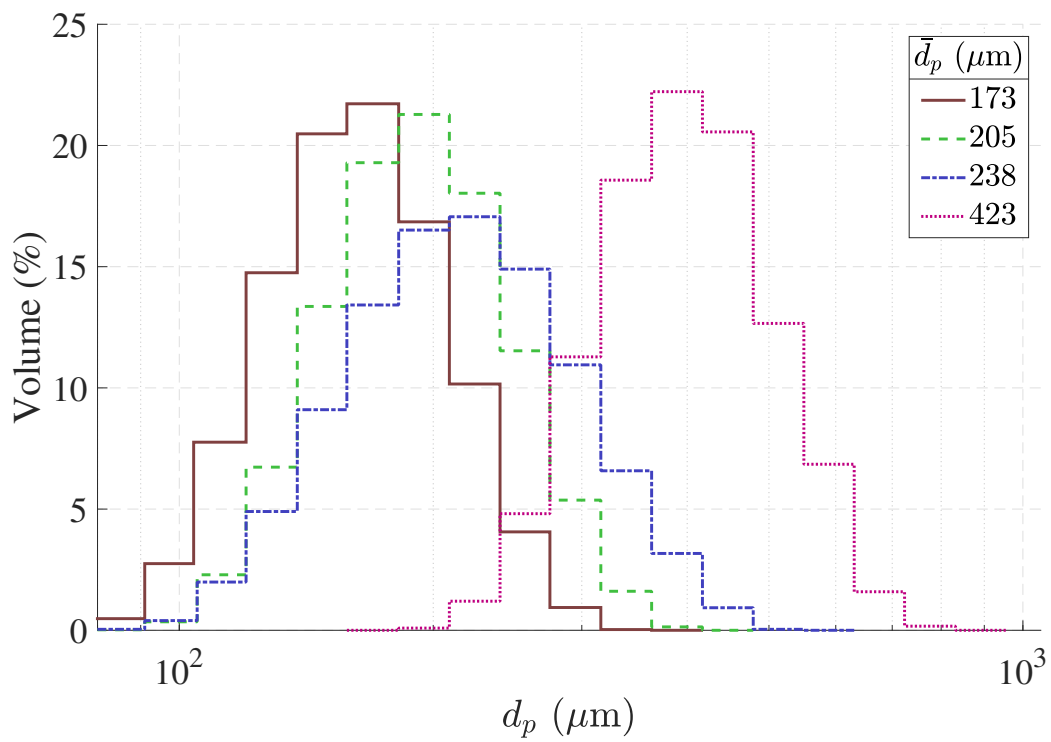


Figure 2: Particle diameter distributions measured using a Malvern Master-sizer 2000.

ive heating beam was generated with a solid-state solar thermal simulator (SSSTS). The SSSTS combines the output from a bundle of infra-red (910 nm) diode lasers using fibre-optics (Alwahabi et al. 2016) to provide a collimated beam at output powers up to  $\dot{Q}_0 = 2840$  W with an approximate diameter of 15 mm at the focal plane, which was aligned with the jet axis 17.6 mm from the exit plane. The intensity profile of the SSSTS beam on the jet axis is described by Lewis et al. 2021, with an approximate peak heating flux on the beam axis of  $42.8 \text{ MW/m}^2$  when operating at  $\dot{Q}_0 = 2840$  W. The beam powers used for the current experiments are listed in Table 1. A water-cooled power meter (Gentec model HP100A-4KW-HE) operating at 10 Hz, positioned down-beam from the wind tunnel, measured the power of the SSSTS that was transmitted through the flow,  $\dot{Q}_{tr}$ . The total power absorbed by the particles was then estimated using the equation  $\dot{Q}_{abs} = \alpha(\dot{Q}_0 - \dot{Q}_{tr})$ , where  $\alpha \approx 0.89$  is the absorptivity of the particles (Siegel et al. 2014). This calculation uses the assumption that multiple scattering of the heating beam does not significantly increase the absorbed fraction and that the emitted radiation from the heated particles does not influence the measured power.

Optical filtering was used to separate the fluorescence emissions and scattering from the particles into two channels for two-colour LIF with central wavelengths of 285 nm and 315 nm, named here  $S_{285}$  and  $S_{315}$ , respectively. One channel to image the scattering of the 532 nm laser sheet by particles was also separated, named  $S_{532}$  here. Each of the three channels were positioned on the same side of the wind tunnel and shared the same optical path through the flow. Long-pass filters were used to suppress the scattered 266 nm laser light, with two beam-splitters positioned in series with cut-off wavelengths of 310 nm and 355 nm used to separate the three channels. The positioning of the cameras and beam-splitters can be seen in Figure 1. Additional filters were used to limit the transmitted signal to narrow spectral bands. The details of filters used and the resultant transmission for each channel are presented by Lewis et al. 2021. Each channel was imaged using a separate camera and lens. Two PC Di-Cam intensified s-CMOS cameras imaged the two fluorescence channels with the signal for the channel  $S_{285}$  focussed using a spherical UV lens ( $f = 100$  mm, Thorlabs LB4821) and for  $S_{315}$  using a Soder UV 100 mm F/2.8 lens. A PCO.2000 CCD with a Tamron macro 80-120 mm lens was used to image  $S_{532}$ . Each camera imaged the measurement region of  $0.3 < x/D < 3.7$ ,  $|r/D| < 1$ , where  $x$  is the axial co-ordinate of the jet and  $r$  is the radial co-ordinate parallel to the laser sheet.

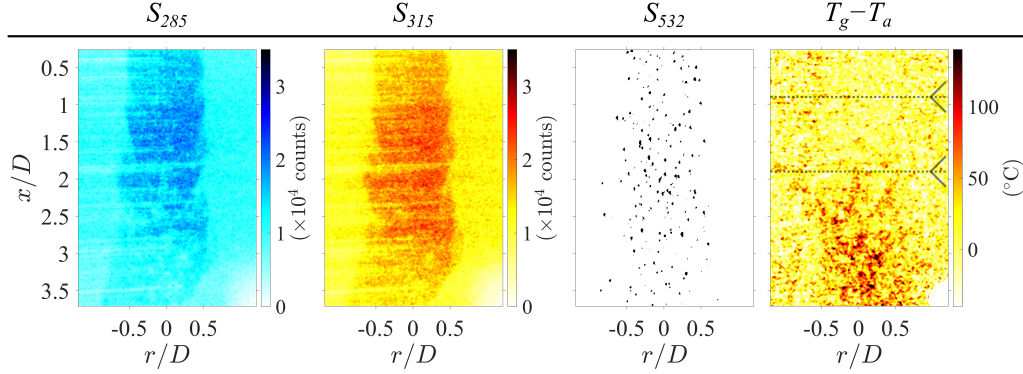


Figure 3: Example instantaneous images taken simultaneously with the two fluorescence cameras,  $S_{285}$  and  $S_{315}$ , the binary mask of particle locations determined from the scattering image  $S_{532}$ , and the resultant temperature calculated from the fluorescence intensity ratio  $S_{315}/S_{285}$ . For this figure and following figures including images of the temperature, the dashed lines and arrows indicate the approximate boundaries and direction of the SSSTS heating beam, respectively.

## 2.2 Image processing

The raw images collected simultaneously from the three cameras were processed using a series of in-house Matlab codes to derive the gas temperature and particle number densities. Examples of the instantaneous images from each camera, together with the calculated gas-phase temperature, are presented in Figure 3. Each step of the process is described in detail by Lewis et al. 2021, so that only a summary is presented here. Firstly, the average background signal, collected with the lasers on and camera uncapped but without a flow, was subtracted from the raw images. A common target grid was then imaged with each camera to spatially align the images from the three channels to within approximately  $\pm 1$  pixel. The alignment of the fluorescence channels was then improved to approximately  $\pm 0.3$  pixels using time-averaged images of the fluorescence emissions from the toluene-seeded jet without heating. This was done by systematically offsetting the image from  $S_{285}$  in increments of 0.1 pixel and calculating the signal ratio  $S_{315}/S_{285}$  on a pixel-by-pixel basis. Because these measurements were conducted under ambient conditions, the true value of  $S_{315}/S_{285}$  should be constant across the field of measurement. Therefore, the image sub-pixel offset location with the smallest variation in the calculated signal ratio was then used to correct all instantaneous images taken on that particular day.

Following spatial alignment, the signal ratio  $S_{315}/S_{285}$  was calculated on

a pixel-by-pixel basis for each instantaneous image. Data from  $S_{285}$  or  $S_{315}$  with a signal of less than 15 times the camera dark charge were removed from further analysis to reduce the influence of camera noise on the measurement (Lewis et al. 2020). The ratio  $S_{315}/S_{285}$  was then converted to temperature using a calibration curve. The calibration was performed in the same jet flow as for the main experiments, except that the jet flow was heated using a controllable electrical tape heater (Briskheat BWH052100LD) fitted to the outside of the central pipe. The heated flow was imaged using  $S_{285}$  and  $S_{315}$  at a series of specified temperatures, with the actual flow temperature measured simultaneously using a thermocouple. The time- and spatially-averaged ratio  $S_{315}/S_{285}$  was then calculated from the potential core region of the jet where the temperature was uniform. The results for the calibration are presented by Lewis et al. 2021, with the relationship between  $S_{315}/S_{285}$  and temperature well described by a linear function for the temperature range expected in the main experiment of  $20\text{ }^{\circ}\text{C} < T_g < 160\text{ }^{\circ}\text{C}$ . After conversion to temperature, the instantaneous images were smoothed using a  $5 \times 5$  pixel median filter to reduce the influence of camera shot noise on the results. The uncertainty of the two-colour LIF method in a particle-laden flow with  $\bar{d}_p = 173\text{ }\mu\text{m}$  and  $\bar{\phi} = 1.4 \times 10^{-3}$ , evaluated using the above methods, was found to have a pixel-to-pixel standard deviation in the instantaneous measured temperature of  $17.8\text{ }^{\circ}\text{C}$  for the  $\bar{d}_p = 173\text{ }\mu\text{m}$  particles (Lewis et al. 2021). This can be reduced through time-averaging, such that for the mean results the error is expected to be  $< 2\text{ }^{\circ}\text{C}$  for each case.

The instantaneous images of scattering from particles ( $S_{532}$ ) were formed into a binary mask using a threshold of 10 times the standard deviation of the dark charge, to ensure the particle signals were strongly separated from the background noise. Individual particle locations were then determined from the binary image, using an in-house Matlab code to separate overlapping particles where possible.

### 3 Analytical models

#### 3.1 One-dimensional heat transfer model

A one-dimensional analytical heat transfer model to estimate the particle and gas temperatures in the jet flow was developed, similar to that presented by Kueh et al. 2018. Both the radiative and convective heat transfer, together with the corresponding change in particle and gas temperature, were calculated for a single spherical particle and the surrounding volume of gas moving axially along the jet centreline. The heat gained by the particle ( $\dot{Q}_{p,gain}$ )

is dependent on the incident radiation absorbed ( $\dot{Q}_{abs}$ ), emitted radiation ( $\dot{Q}_{emit}$ ) and convection with the surrounding fluid ( $\dot{Q}_{conv}$ ). The resultant heat transfer balance for the particle is given by the following equation:

$$\dot{Q}_{p,gain} = \dot{Q}_{abs} - \dot{Q}_{conv} - \dot{Q}_{emit} = \frac{\alpha \pi d_p^2 \dot{Q}_{rad}''}{4} - h \pi d_p^2 (T_p - T_f) - \epsilon \sigma \pi d_p^2 (T_p^4 - T_a^4), \quad (1)$$

where  $\alpha$  is the absorptivity of the particle and  $\dot{Q}_{rad}''$  is the incident radiative heat flux. The convective heat transfer coefficient is  $h = Nu k_{film}/d_p$ , where  $Nu$  is the Nusselt number of the particle and  $k_{film}$  is the thermal conductivity of the fluid evaluated at the film temperature. The Nusselt number for a sphere in forced convection is given by:

$$Nu = 2 + (0.4 Re_p^{1/2} + 0.06 Re_p^{2/3}) Pr^{0.4}, \quad (2)$$

where the Reynolds and Prandtl numbers of the particle are

$$Re_p = \rho_{film} |U_{slip}| d_p / \mu_{film} \quad (3)$$

and

$$Pr = c_{p,f} \mu_{film} / k_{film} \quad (4)$$

respectively. Here,  $c_{p,f}$  is the specific heat of the fluid while  $\rho_{film}$  and  $\mu_{film}$  are the fluid's respective density and dynamic viscosity evaluated at the film temperature. The slip velocity  $U_{slip} = U_f - U_p$  is the instantaneous difference between the local fluid and particle velocities. The emitted radiation is a function of the particle emissivity,  $\epsilon$ , and the Stefan-Boltzmann constant  $\sigma = 5.67 \times 10^{-8} \text{ W/m}^2\text{K}^4$ . The particle, fluid and ambient temperatures are represented by  $T_p$ ,  $T_f$  and  $T_a$  respectively. The resultant rate of particle temperature change with time ( $t$ ) can then be calculated from the following equation:

$$\frac{\partial T_p(t)}{\partial t} = \frac{6}{d_p c_{p,p} \rho_p} \left[ \frac{\alpha}{4} \dot{Q}_{rad}''(t) - h (T_p(t) - T_f(t)) - \epsilon \sigma (T_p^4(t) - T_a^4) \right], \quad (5)$$

where  $c_{p,p}$  is the specific heat of the particle and  $\rho_p$  is the particle density. The local radiative heat flux varies with time as the particle travels through the heating region because of the profile of the heating beam. This is modelled using the measured profile of the heating beam, presented by (Lewis et al. 2021), and the particle trajectory through the region. For the special case of a uniform particle velocity we obtain  $\dot{Q}_{rad}''(t) = \dot{Q}_{rad}''(x/U_p)$ , where  $U_p$  is the particle velocity in the  $x$  direction. The subsequent gas temperature change,

using the assumption that all convective thermal energy is transferred to the gas, is given by:

$$\frac{\partial T_f(t)}{\partial t} = \frac{6h\phi}{d_p c_{p,f} \rho_{film}} (T_p(t) - T_f(t)). \quad (6)$$

In the model, the particle volumetric loading of the flow was assumed to be uniform and constant to match the jet exit values used in the experiments. A constant slip velocity ratio of  $U_{slip} = 0.2U_f$  was used, approximated from the value measured by Gillandt et al. 2001 for particles with  $\bar{d}_p = 110 \mu\text{m}$  and  $\rho_p \approx 2000 \text{ kg/m}^3$  at a loading of  $\phi \approx 5 \times 10^{-4}$ . Attenuation of the radiation up-beam from the particle assumed to be negligible. The values for specific heat capacity (as a function of particle temperature), absorptivity and emissivity were estimated from those measured for similar particles (Chen et al. 2006; Siegel et al. 2014; Siegel et al. 2015). The carrier fluid was modelled as pure nitrogen with the density, viscosity and specific heat calculated as a function of the fluid temperature (Incorpera et al. 2007). The model input parameters are summarised in Table 2.

Figure 4 presents the axial evolution of calculated temperatures of the particle- and gas-phase (a), together with the corresponding values of the absolute power of each heat transfer process (b), for the case with  $\bar{d}_p = 173 \mu\text{m}$ ,  $\bar{\phi} = 1.4 \times 10^{-3}$  and  $\dot{Q}_0 = 2840 \text{ W}$  (note that data on the y-axis for the heat transfer powers are presented on a logarithmic scale). It can be seen that the particle temperature on the jet centreline is calculated to increase rapidly throughout the heating region, reaching a peak of approximately 300 °C at the downstream edge. The particle temperature is predicted to be much higher than that of the gas throughout the measurement. This is consistent with the radiative energy absorbed by particles in the heating region,  $0.9 < x/D < 1.9$ , being some two orders of magnitude greater than that transferred from the particles, either by radiation or from convection with the gas. The difference can be seen in the bottom sub-figure with  $\dot{Q}_{abs} > 100 \times \dot{Q}_{conv}$  and  $\dot{Q}_{abs} > 1000 \times \dot{Q}_{emit}$  at  $x/D = 1.4$ . Downstream from the heating region, the difference between the particle and gas temperatures decreases with axial distance toward equilibrium, although this is far downstream from the region of investigation. In the region of  $1 < x/D < 4$  convection is predicted to be the dominant mode of particle cooling, with  $\dot{Q}_{conv} > 10 \times \dot{Q}_{emit}$ .

Table 2: Input parameters used for the analytical heat transfer model. The particle properties used were those previously measured for the Carbobead CP particles or similar. The properties used for the gas were those of pure nitrogen. Temperature dependent parameters are indicated within the brackets in the Symbol column.

Parameter	Symbol	Value
Peak heating flux	$\dot{Q}_{peak}''$	13.7, 29.4, 36.3, 42.8 MW/m <sup>2</sup>
Particle diameter	$d_p$	173, 205, 238, 423 $\mu\text{m}$
Particle volumetric loading ( $\times 10^{-3}$ )	$\phi$	0.625, 1, 1.4
Particle density	$\rho_p$	3270 kg/m <sup>3</sup>
Particle specific heat	$c_{p,p}(T_p)$	0.7-1.1 kJ/kgK
Particle absorptivity	$\alpha$	0.89
Particle emissivity	$\epsilon$	0.85
Particle velocity	$U_p$	2.9 m/s
Fluid velocity	$U_f$	3.6 m/s
Fluid density	$\rho_f(T_f)$	1.1-0.8 kg/m <sup>3</sup>
Fluid viscosity	$\mu_f(T_f)$	1.8-2.2 $\times 10^{-5}$ Ns/m <sup>2</sup>
Fluid specific heat	$c_{p,f}(T_f)$	1.04 kJ/kgK
Ambient temperature	$T_a$	20 °C

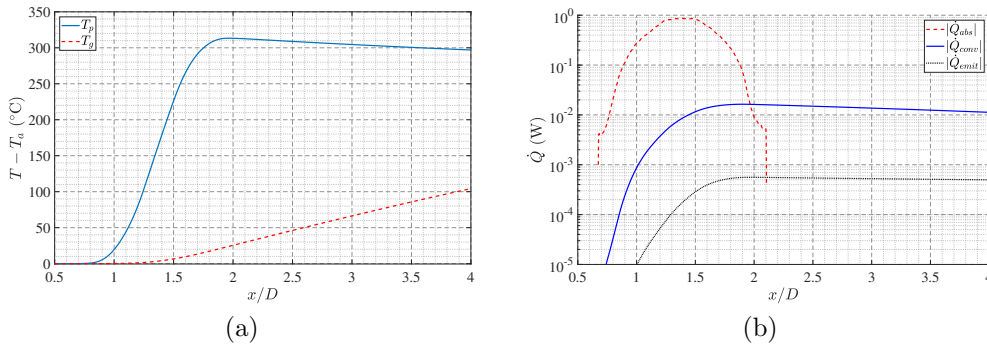


Figure 4: The simulated temperature from the one-dimensional model of both the particle and gas (a) together with the absolute powers of the modelled particle heat transfer components (b) as a function of axial distance, for the parameters listed in Table 2 with  $\bar{d}_p = 173 \mu\text{m}$ ,  $\bar{\phi} = 1.4 \times 10^{-3}$  and  $\dot{Q}_0 = 2840 \text{ W}$ .

### 3.2 Heating beam attenuation model

The absorption of the heating beam by the particles was predicted numerically using a simplified attenuation model. The model generates a random distribution of particles in a cylindrical spatial domain with both a length and diameter of  $1.5D$  positioned such that the centre of the domain coincided with the intersection of the jet axis and that of the SSSTS beam. The particle locations were modelled using a weighted distribution such that the radial profiles of particle number density matched those previously reported for the case with  $\bar{d}_p = 173 \mu\text{m}$  (Lewis et al. 2021). The number of particles in the domain was also selected such that the average volumetric loading matched the experimental cases. Particles were modelled as spheres with a particle size distribution matching that of the present experiment (see Figure 2). Any modelled particles that overlapped in the 3-D space were removed and iteratively replaced until there was no overlap. A 2-D binary mask of the particle locations, projected in the direction of the laser, was then generated with the domain discretised into pixels with sides of length  $0.001D$ . This length was sufficiently small for the results to converge. The spatial distribution of heating laser flux in each resulting pixel was then calculated using the profile presented by Lewis et al. 2021. Figure 5 presents a typical distribution of the modelled particle locations, for the case with particles of  $\bar{d}_p = 423 \mu\text{m}$  at a volumetric loading of  $\phi = 1.4 \times 10^{-3}$ , together with the intensity profile of the SSSTS beam and the particle cross-sectional area projected in the beam direction. Here,  $x$  is the axial co-ordinate of the jet, while  $r$  and  $y$  are the radial co-ordinates parallel and perpendicular to the heating laser beam direction, respectively. The simulated transmission and attenuation of the heating beam through the flow was then calculated from the element-wise multiplication of the heating flux and the binary mask of projected particles, using the assumption that the particle transmissivity, forward scattering and multiple scattering were negligible.

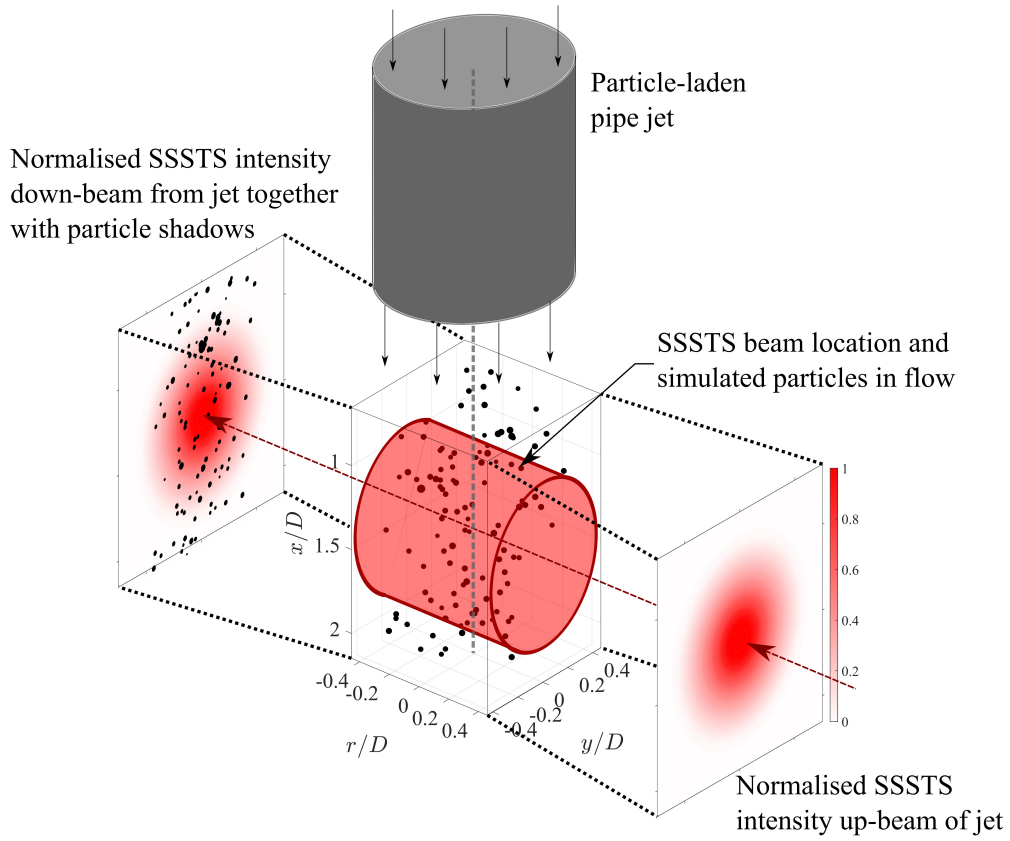


Figure 5: Schematic diagram illustrating the method used to model the attenuation of the SSSTS heating beam. An example of the distribution of the simulated particle locations is shown for the case with  $\bar{d}_p = 423 \mu\text{m}$  and  $\phi = 1.4 \times 10^{-3}$ , together with the intensity of the heating beam.

## 4 Results

Figure 6 presents typical instantaneous images of the measured temperature above ambient ( $T_g - T_a$ ), the binary particle mask and the fluorescence intensity from  $S_{285}$ , for each particle size distribution. The particle volumetric loading for each image was  $\phi = 1.4 \times 10^{-3}$  with a SSSTS beam power of  $\dot{Q}_0 = 2840$  W. Additionally, one reference case without heating for the  $\bar{d}_p = 406$   $\mu\text{m}$  particles is presented to show the accuracy of the method. The largest particle case was chosen because the reduction in signal due to attenuation, and therefore also the random error, increases with  $d_p$ . The dashed lines and arrows overlaying the temperature images indicate the approximate boundaries and direction of the SSSTS heating beam, respectively.

Several qualitative trends can be seen from the temperature images with the heating laser switched on. The gas temperature can be seen to increase with a reduction in particle size, so that it is greatest for the particles with  $\bar{d}_p = 173$   $\mu\text{m}$ . This is as expected because the radiation absorption and convective heat transfer increase with total particle cross-sectional area and surface area, respectively, and hence with decreasing particle size for a constant  $\phi$ . The instantaneous distributions of temperature can also be seen to be highly non-uniform in the flow downstream from the heating region, with large-scale coherent regions of high temperature evident for each case with heating. This indicates that the gas is not well mixed, even at the downstream edge of these images, and is also consistent with the particles being distributed with regions of high local volumetric loadings whose position relative to the gas is persistent (i.e., long lived). These local regions of high temperature become more prevalent with decreasing  $\bar{d}_p$ , with the temperature difference from the surrounding flow also increasing. More hot regions can be seen on the heating laser in-side of the image, for  $r/D > 0$ , suggesting that attenuation of the radiation significantly affects the temperature distribution of the flow.

Spatial variations of the fluorescence intensity can be seen throughout the images, driven by the mixing of the jet flow with the surroundings together with the non-uniform laser sheet intensity profile. Temporal changes in the toluene concentration from case to case can also be seen to affect the fluorescence intensity. These variations in signal are corrected for in the temperature measurement because the temperature is derived from the ratio of fluorescence emissions, as described above. However, the influence of random errors increases with decreasing signal. Attenuation of the excitation laser and signal trapping can be seen in the fluorescence images as streaks and circular regions with low intensity, respectively. The size of these regions of reduced intensity increases with particle diameter. The worst case attenuation is for the  $\bar{d}_p = 423$   $\mu\text{m}$  particles, for which the fluorescence signal inside these

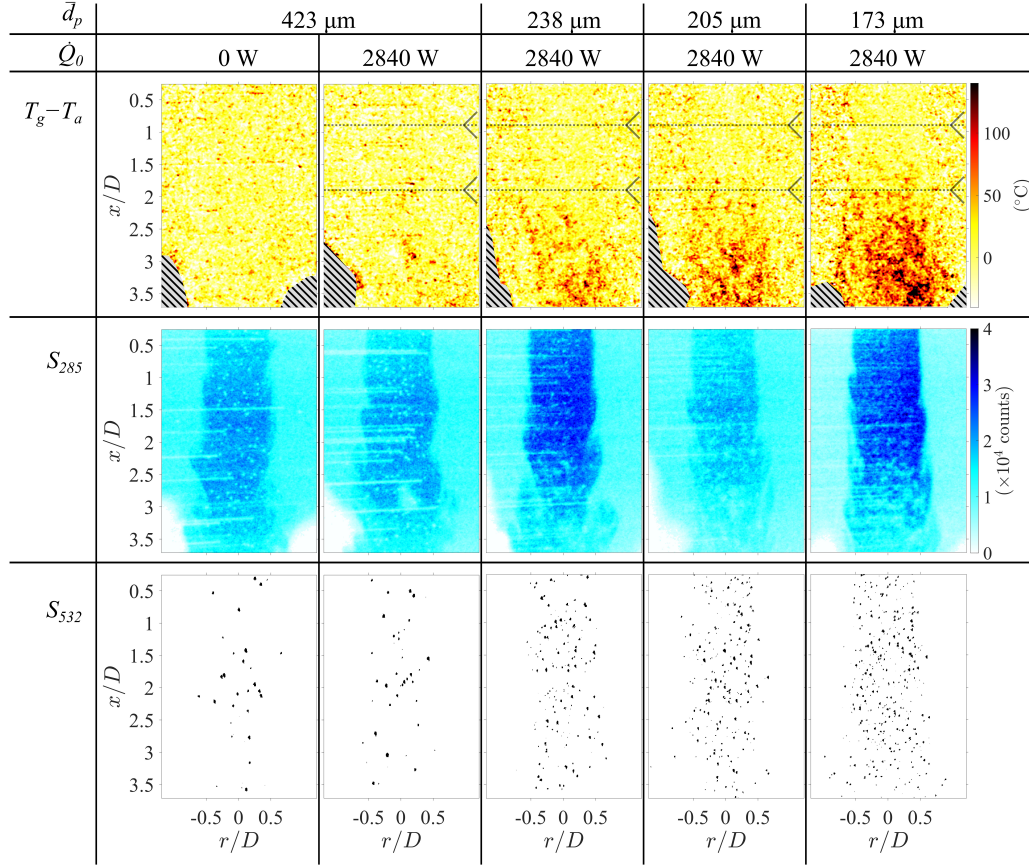


Figure 6: Typical instantaneous images of the calculated temperature, fluorescence intensity and binary particle mask, measured simultaneously, for each particle size with  $\phi = 1.4 \times 10^{-3}$  and  $\dot{Q}_0 = 2840$  W. Also presented is a reference case without heating, for the  $\bar{d}_p = 406$   $\mu\text{m}$  particles. The dotted lines represent the upper and lower extent of the heating laser, where used, while the arrow-head shows its direction. The hatched areas correspond to regions where the signal from one or both of the fluorescence images is below the threshold for reliable measurements.

streaks is reduced by up to 45% compared to their surroundings. Despite the significant variation in fluorescence signal from these combined sources, the pixel-to-pixel standard deviation of the calculated ratio  $S_{315}/S_{285}$  for the case without heating in the region  $1 < x/D < 2$ ,  $|r/D| < 0.3$  is  $0.076 \times S_{315}/S_{285}$ , corresponding to a temperature uncertainty of 18.8 °C. This is a 6% increase of the uncertainty compared to that measured previously for the  $\bar{d}_p = 173 \mu\text{m}$  particles of 17.8 °C (Lewis et al. 2021). These uncertainties were calculated from the images of the flow without heating, with a known, uniform temperature. The uncertainty is expected to increase with temperature because the fluorescence intensity decreases with an increase in temperature. The effect of temperature on the uncertainty was estimated using images of the unheated flow, with the laser power reduced such that the fluorescence intensity matched that measured for the case with the highest heating. The resultant uncertainty for the time-averaged images, to one standard deviation, is estimated to be less than 5 °C for each case across the majority of the image bounded by the region  $0.5 < |r/D|$ ,  $0.5 < x/D < 3.7$ .

Figure 7 presents the time-averaged temperature above ambient,  $\bar{T}_g - T_a$ , for each particle size with  $\bar{\phi} = 1.4 \times 10^{-3}$  and  $\dot{Q}_0 = 2840 \text{ W}$ . The trends seen in Figure 6 are also evident here, with the mean temperature downstream of the heating region increasing with a decrease in particle size and a greater temperature rise for the laser-in side, for  $r/D > 0$ , than for  $r/D < 0$ . The temperature within the main jet flow, for  $|r/D| < 0.5$ , can be seen to be greater than the ambient from the start of the heating region, with  $\bar{T}_g - T_a$  increasing with  $x/D$  to the downstream edge of the image. The majority of the temperature rise is constrained within  $|r/D| < 0.6$ , suggesting there is little spreading of the jet and/or mixing with the co-flow to the downstream edge of the measurement region. Only one heating flux and loading is presented here because the trends are similar for all cases, with the presented conditions chosen because they exhibit the greatest temperature change.

Figure 8 presents the time-averaged temperature images for a series of particle volumetric loadings for the case with  $\bar{d}_p = 205 \mu\text{m}$  and  $\dot{Q}_0 = 2840 \text{ W}$ . Note the condition of  $\bar{\phi} = 1.4 \times 10^{-3}$  is repeated from Figure 7, although the colour scale is different. The temperature rise downstream from the heating region increases with particle loading, which is as expected because the greater cross-sectional and surface area of particles leads to an increase in the total radiation absorption and convective heat transfer, respectively.

Figure 9 presents the power from the SSSTS beam that was transmitted through the particle-laden flow,  $\dot{Q}_{tr}$ , normalised by the initial beam power,  $\dot{Q}_0$ , as a function of particle diameter for a series of volumetric loadings with  $\dot{Q}_0 = 2840 \text{ W}$ . Both the measured and simulated transmissions are presented. It can be seen that  $\dot{Q}_{tr}/\dot{Q}_0$  decreases with an increase in  $\bar{\phi}$  and a decrease in

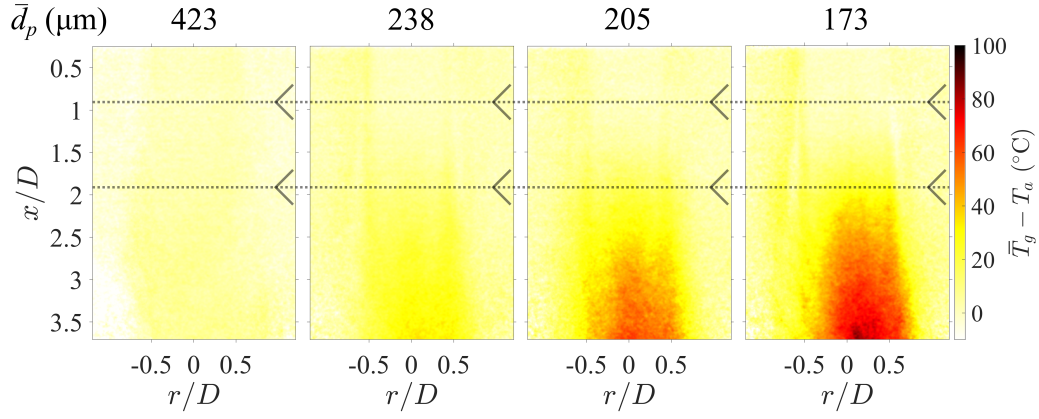


Figure 7: Time-averaged gas-phase temperature distributions for each of the four particle sizes distributions with a fixed particle volumetric loading of  $\bar{\phi} = 1.4 \times 10^{-3}$  and a constant power of the heating laser of  $\dot{Q}_0 = 2840$  W.

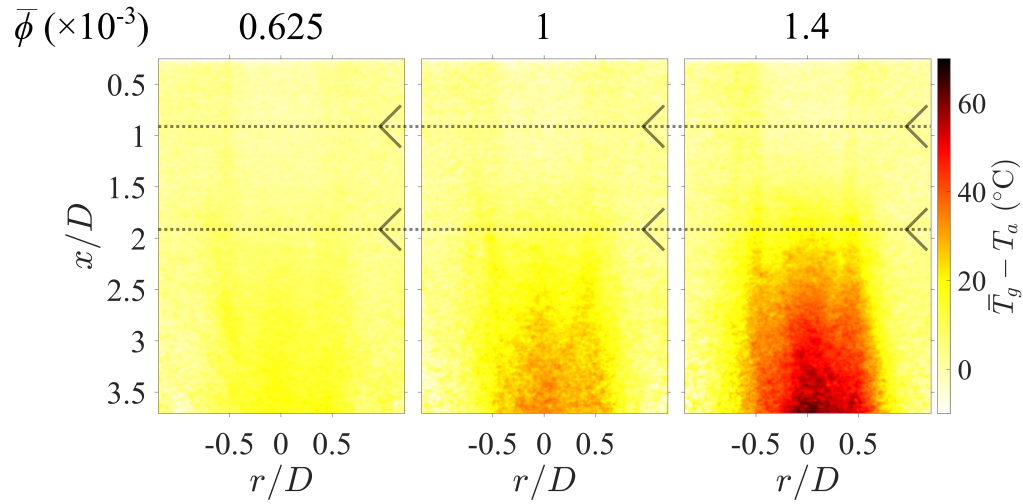


Figure 8: Time-averaged gas-phase temperature distributions for a series of particle volumetric loadings for the particles with  $\bar{d}_p = 205$  μm and  $\dot{Q}_0 = 2840$  W.

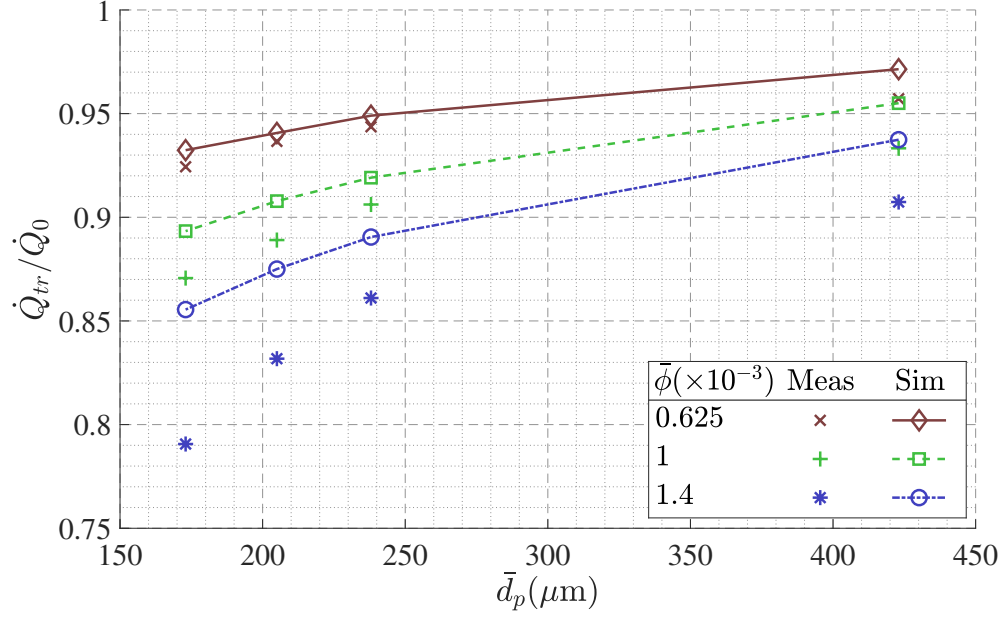


Figure 9: Comparison of the measured (Meas) and simulated (Sim) power of the SSSTS beam transmitted through the particle-laden flow, normalised by the total beam power, as a function of particle diameter for each volumetric loading investigated. The measured results presented are for the cases with  $\dot{Q}_0 = 2840$  W.

$\bar{d}_p$ , which is consistent with the results presented in Figure 7 and Figure 8. This is because the total cross-sectional area of particles in the flow increases with an increase in  $\bar{\phi}$  for constant  $\bar{d}_p$  and a decrease in  $\bar{d}_p$  for constant  $\bar{\phi}$ , resulting in a greater absorption of the heating beam by particles. The lowest measured transmission of the SSSTS beam was  $\dot{Q}_{tr}/\dot{Q}_0 = 0.79$  for the particles with  $\bar{d}_p = 173 \mu\text{m}$  at a volumetric loading of  $\bar{\phi} = 1.4 \times 10^{-3}$ . This corresponds to an approximate absorption of the beam by particles of  $\dot{Q}_{abs}/\dot{Q}_0 = 0.19$ .

The results seen for the measured transmission match sufficiently well with the simulated values calculated using a random distribution of particles to have good confidence in the trends. For each case the measured transmission is lower than that calculated from the model, with the difference increasing with  $\bar{\phi}$  for all cases of  $\bar{d}_p$  investigated. There are several possible reasons for this discrepancy. These include that the particles are simulated as spherical, whereas the specified sphericity of the particles by the manufacturer is 0.9. The area-to-volume ratio of particles in the flow increases

with decreasing sphericity, leading to an increase in the amount of radiation being attenuated by particles. Breakage of particles or abrasion that generates fine particles in the system could lead to a decrease in the average diameter of particles in the flow relative to that measured, without changing the volumetric loading. This would be more significant for higher loadings because of greater stresses in the feeding system and the increased likelihood of particle-particle collisions in the conveying pipes and jet flow. Additionally, fine particles that occupy a very small volume percent but relatively larger number density may not be recorded when measuring the particle diameter distribution. While these complexities in the real system are not easily predicted or incorporated in models, their contribution is also expected to be modest.

Figure 10 presents the time-averaged temperature above ambient measured on the jet centreline as a function of axial distance for a series of heating powers with  $\bar{d}_p = 205 \mu\text{m}$  and  $\bar{\phi} = 1.4 \times 10^{-3}$  (a), a series of particle volumetric loadings with  $\bar{d}_p = 205 \mu\text{m}$  and  $\dot{Q}_0 = 2840 \text{ W}$  (b), and a series of particle diameters with  $\bar{\phi} = 1.4 \times 10^{-3}$  and  $\dot{Q}_0 = 2840 \text{ W}$  (c). Note that the case for the particles with  $\bar{d}_p = 205 \mu\text{m}$ ,  $\bar{\phi} = 1.4 \times 10^{-3}$  and  $\dot{Q}_0 = 2840 \text{ W}$  is presented in each subfigure. The inset in each sub-figure presents the axial profile of the centreline temperature rise relative to the power absorbed by particles,  $(\bar{T}_g - T_a)/\dot{Q}_{abs}$ . This gives a measure of how efficiently the absorbed radiative energy is transferred to the gas-phase. The trends seen in the normalisation are expected to be reliable even though there is some uncertainty in the absolute values owing to the uncertainty in some of the data used to estimate  $\dot{Q}_{abs}$ , because the particle material properties are the same for each case.

The general trends seen in the time-averaged images are confirmed here, with the temperature increasing monotonically from  $x/D \approx 1.1$  to the downstream edge of the measurement region for all cases with heating and  $\bar{T}_g - T_a$  increasing with an increase in  $\dot{Q}_0$ , an increase in  $\bar{\phi}$  and a decrease in  $\bar{d}_p$ . The increase in temperature with axial distance is close to linear for  $1.9 < x/D < 3.7$ , indicating that the convective heat transfer is nearly constant downstream from the heating beam to the edge of the measurement region. This suggests that the particle temperature after radiative heating remains significantly greater than that of the fluid throughout this region, which agrees well with the trends obtained from the analytical model in Figure 4.

The normalised axial temperature profile  $(\bar{T}_g - T_a)/\dot{Q}_{abs}$  collapses well for  $x/D < 2.5$  for each heating power. This shows that the temperature rise in this region is proportional to the power absorbed by the particles, for a constant particle diameter and volumetric loading. This is because the particle temperature rise is directly proportional to the radiative flux and the

subsequent temperature rise of the gas is proportional to the temperature differential between the particles and gas,  $T_p - T_g$ . The trends calculated with the analytical model (see Figure 4) predict that  $T_p \gg T_g$  in the region  $1.9 < x/D < 2.5$ , which would lead to an almost constant rate of convective heat transfer in this region. Downstream from this region, for  $x/D > 2.5$ , the relative temperature increase  $(\bar{T}_g - T_a)/\dot{Q}_{abs}$  can be seen to decrease slightly with increasing heating beam power. This is potentially because buoyancy-induced mixing/convection within the gas-phase increases with an increase in the gradients of temperature in the flow. In the region  $1.9 < x/D < 2.5$ , the value of  $(\bar{T}_g - T_a)/\dot{Q}_{abs}$  also collapses well for the series of values of  $\bar{\phi}$ , although downstream from this region the value of  $(\bar{T}_g - T_a)/\dot{Q}_{abs}$  increases with  $\bar{\phi}$ . This suggests that, while the heat absorbed by the particles and initial heat transfer is proportional to the volumetric loading, increasing the volumetric loading also decreases the radial gas-phase transport. In the region  $x/D > 1.5$ ,  $(\bar{T}_g - T_a)/\dot{Q}_{abs}$  increases significantly with decreasing particle diameter for  $\bar{d}_p \geq 205 \mu\text{m}$ . However,  $(\bar{T}_g - T_a)/\dot{Q}_{abs}$  was found to be similar for the particles with  $\bar{d}_p = 173$  and  $205 \mu\text{m}$ . These trends are consistent for all heating powers and volumetric loadings investigated. This demonstrates the non-linear nature of the relationships between the particle diameter and the convective and radiative heat transfer processes in the flow.

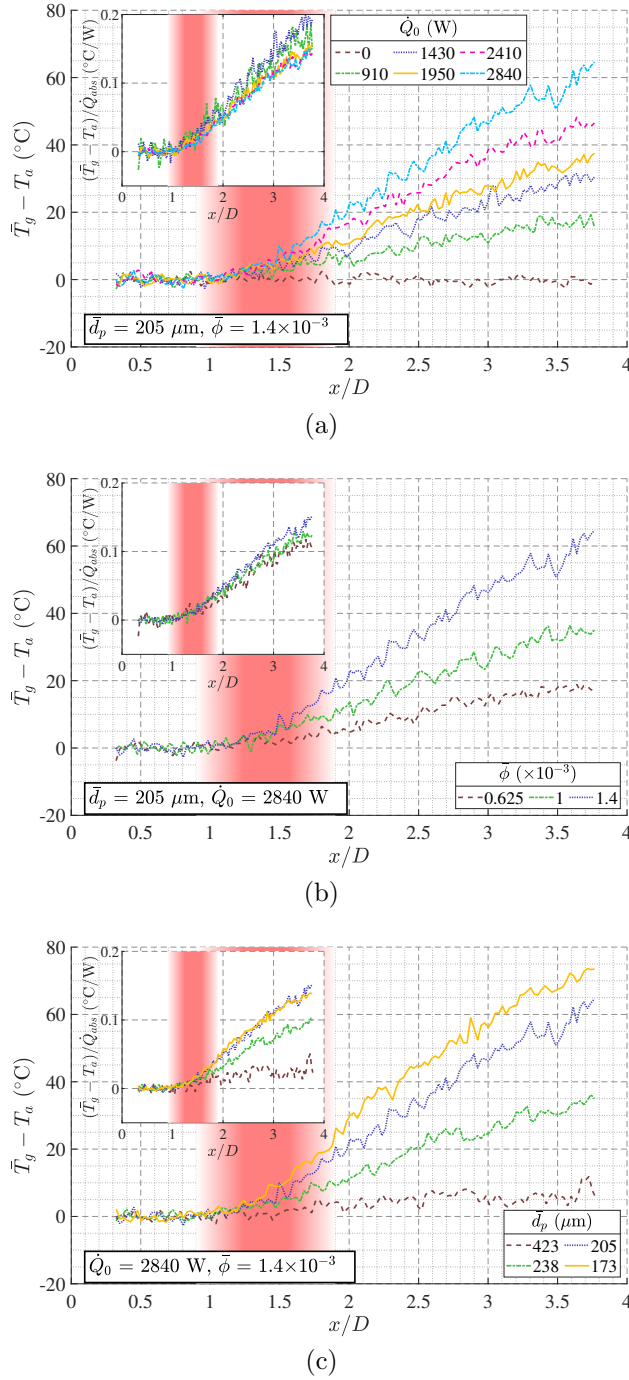


Figure 10: Measured temperature above ambient on the jet centreline for a series of heating fluxes (a), particle loadings (b) and particle diameters (c). The inset in each figure presents the temperature above ambient normalised by the estimated absorbed power.

Figure 11 presents the measured and calculated values of the rate of change of the gas temperature with axial distance on the jet centreline,  $dT_g/dx$ , averaged over the region of  $2 < x/D < 3$ . The results are presented for a series of particle diameter distributions as a function of  $\dot{Q}_0$  with  $\bar{\phi} = 1.4 \times 10^{-3}$  (a) and as a function of  $\bar{\phi}$  with  $\dot{Q}_0 = 2840$  W (b). The measured axial temperature gradient  $dT_g/dx$  can be seen to increase approximately linearly with  $\dot{Q}_0$  and monotonically with  $\bar{\phi}$  in this region. The gradient  $dT_g/dx$  also generally increases with a decrease in  $\bar{d}_p$ , except for the particles with  $\bar{d}_p = 173$   $\mu\text{m}$  for which the gradient is similar to that seen for the particles with  $\bar{d}_p = 205$   $\mu\text{m}$ . For the case with  $\dot{Q}_0 = 2840$  W and  $\bar{\phi} = 1.4 \times 10^{-3}$ ,  $dT_g/dx \approx 2,200$   $^\circ\text{C}/\text{m}$  for  $\bar{d}_p = 173$  and  $205$   $\mu\text{m}$ . This corresponds to a gas-temperature heating rate of approximately  $8,000$   $^\circ\text{C}/\text{s}$ , assuming that the axial gas velocity is constant in this region at the jet exit bulk-mean velocity of  $3.6$  m/s. At this loading and heating power,  $dT_g/dx$  decreases with an increase in particle diameter to  $1,200$  and  $300$   $^\circ\text{C}/\text{m}$  for  $\bar{d}_p = 238$  and  $423$   $\mu\text{m}$ , respectively.

The model can be seen to overestimate the gradient for most investigated fluxes, loadings and particle sizes, except for the case with  $\bar{d}_p = 238$   $\mu\text{m}$ . Furthermore, the magnitude of difference between the experimental measurements and the modelled results increases with a decrease in the particle diameter. One critical parameter in determining convective heat transfer is the slip velocity, which was assumed to be constant at  $U_{slip} = 0.2U_g$  in the model for all cases. There are currently no measurements of both the gas- and particle-phase velocities for the flow conditions and particles used in the experiments, so the value chosen in the model was approximated from that measured for the most similar conditions in the available literature (Gillandt et al. 2001). Additionally, attenuation of the heating beam and particle clustering, which are not accounted for in the model, may change the heat absorbed by particles on the centreline and the subsequent convective heat transfer. Despite these simplifications the trends seen in the model are in good agreement with the experimental results, with the model overestimating the gradient by  $19.6\%$  on average for the cases with  $dT_g/dx > 500$   $^\circ\text{C}/\text{m}$ .

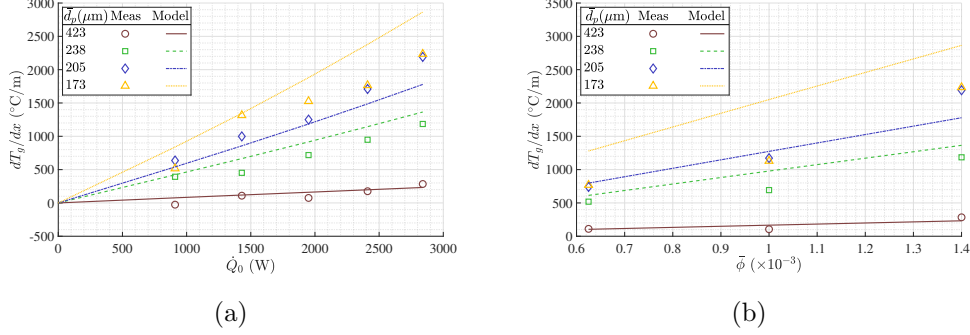


Figure 11: Average rate of temperature increase with axial distance on the jet centreline over the region  $2 < x/D < 3$ , for both the measurements and the one-dimensional model, as a function of heat flux for each particle diameter with  $\bar{\phi} = 1.4 \times 10^{-3}$  (a) and as a function of volumetric loading for each particle diameter with  $\dot{Q}_0 = 2840$  W (b).

Figure 12 presents the measured radial profiles of the gas-phase temperature above ambient at  $x/D = 3$  for a series of heating powers with  $\bar{d}_p = 205$   $\mu\text{m}$  and  $\bar{\phi} = 1.4 \times 10^{-3}$  (a), for a series of particle volumetric loadings with  $\bar{d}_p = 205$   $\mu\text{m}$  and  $\dot{Q}_0 = 2840$  W (b), and for a series of particle diameters with  $\bar{\phi} = 1.4 \times 10^{-3}$  and  $\dot{Q}_0 = 2840$  W (c). The inset in each subfigure presents the radial temperature profile normalised by the estimated heating power absorbed,  $(\bar{T}_g - T_a)/\dot{Q}_{abs}$ . The measured temperature rise  $\bar{T}_g - T_a$  increases with both  $\dot{Q}_0$  and  $\bar{\phi}$ , consistent with previous figures, within the region  $|r/D| < 1$  at this axial location. The temperature can be seen to generally peak near to the jet centreline and decrease with  $|r/D|$ , consistent with the particle loading being greatest there for particles with  $Sk_D \gg 1$  (Lau and Nathan 2016; Lewis et al. 2021). However, for the cases with  $\bar{d}_p = 406$   $\mu\text{m}$  or  $\bar{\phi} \leq 1.4 \times 10^{-3}$ , i.e. the cases with the lowest particle number densities,  $\bar{T}_g - T_a$  can be seen to be close to uniform for  $|r/D| < 0.5$ . The radial profiles for the cases with  $\bar{d}_p \leq 238$   $\mu\text{m}$ ,  $\dot{Q}_0 \geq 1430$  W and  $\bar{\phi} = 1.4 \times 10^{-3}$  also show asymmetry consistent with the influence of attenuation of the heating beam, with  $\bar{T}_g - T_a$  being up to 10 °C greater at  $r/D = 0.3$  than at  $r/D = -0.3$ . This suggests that the average gas-phase temperature at any location will also be dependent on the path length of the heating beam through the flow to that location.

The radial profile of the normalised temperature rise,  $(\bar{T}_g - T_a)/\dot{Q}_{abs}$ , collapses well for the flow with heating powers of  $\dot{Q}_0 \geq 1950$  W, for  $\bar{d}_p = 205$   $\mu\text{m}$  and  $\bar{\phi} = 1.4 \times 10^{-3}$ . For  $\dot{Q}_0 < 1950$  W the normalised temperature can be seen to increase with a decrease in  $\dot{Q}_0$ , although it should be noted that

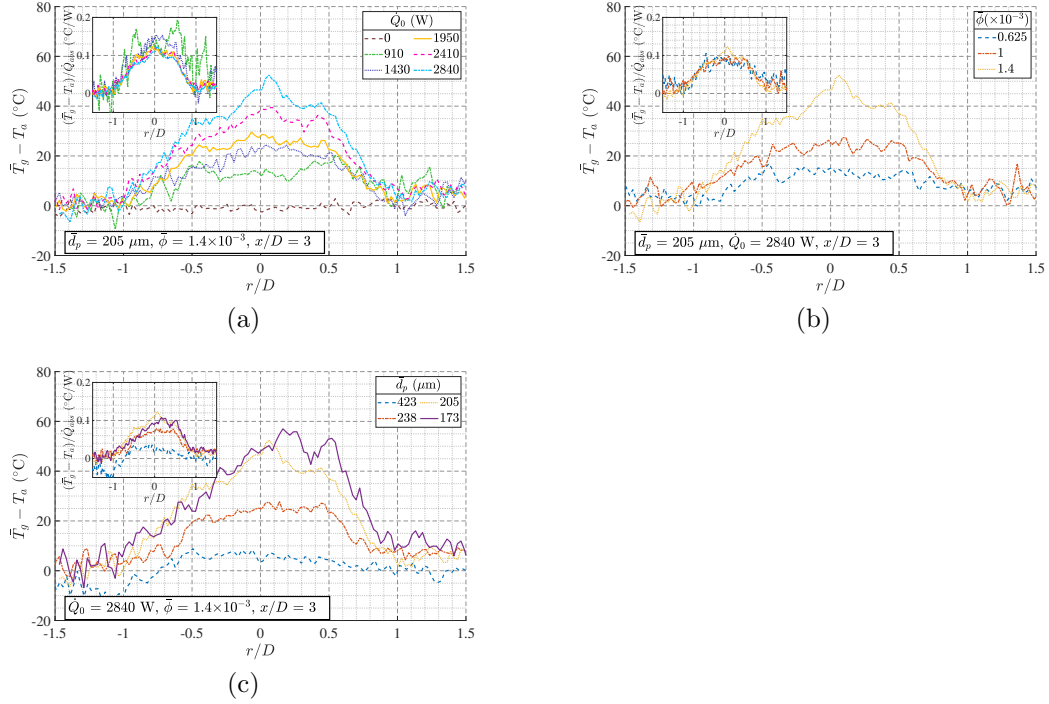


Figure 12: Radial profiles of the temperature above ambient measured at  $x/D = 3$  for a series of heating fluxes with  $\bar{d}_p = 205 \mu\text{m}$  and  $\bar{\phi} = 1.4 \times 10^{-3}$  (a), a series of particle loadings with  $\bar{d}_p = 205 \mu\text{m}$  and  $\dot{Q}_0 = 2840 \text{ W}$  (b), and for a series of particle diameters with  $\dot{Q}_0 = 2840 \text{ W}$  and  $\bar{\phi} = 1.4 \times 10^{-3}$  (c). The inset in each sub-figure presents the respective temperature rise normalised by the estimated absorbed power.

the influence of noisy data (estimated to be  $\pm 5 \text{ }^\circ\text{C}$ ) on this normalisation increases with a decrease in  $\bar{T}_g - T_a$ . As such, there is no clear indication that the mixing/radial transport of the gas-phase is dependent on the heating power at his axial location, although gas-phase velocity measurements are required to confirm this. For each value of  $\bar{\phi}$  the normalised temperature profile is similar in the region outside the main core of the jet, for  $|r/D| > 0.5$ . Nearer to the jet centreline, for  $|r/D| < 0.3$ ,  $(\bar{T}_g - T_a)/\dot{Q}_{abs}$  increases with  $\bar{\phi}$ , suggesting that the radial transport of the gas-phase decreases with an increase in the particle loading. This agrees with previous velocity measurements of the gas phase in a particle-laden jet flow, with the radial velocity fluctuation and turbulence intensity both measured to increase with a decrease in  $\phi$  (Modarress et al. 1984).

## 5 Conclusions

The combination of systematic and spatially-resolved measurements of the gas-phase temperature in a particle-laden jet and an analytical model of heat transfer for a single particle provide strong evidence of the important roles played by both a) large-scale coherent motions and b) the variable spatial distribution of particles in the heat transfer processes in a particle-laden flow heated with high-flux radiation. The agreement between the model and the experiments was also sufficient to provide confidence in the trends and mechanistic explanations for which they were applied.

Images of the instantaneous gas temperature distribution in the radiatively heated particle-laden jet were found to display localised regions that are significantly hotter or colder than the surrounding areas throughout the imaged area, both within and downstream from the heating zone. These correlate visually with regions where a locally high particle volumetric loading can be observed and are qualitatively consistent with the important role of persistent coherent structures in the flow. The number of distinct regions of high/low temperature, and the temperature difference between these regions and their surroundings, was found to increase with a decrease in particle diameter.

The time-averaged gas-phase temperature measured downstream from the radiative heating zone was found to increase with either an increase in particle loading or a decrease in particle diameter. This is consistent with the total radiation absorption and the subsequent convective heat transfer being proportional to the total cross-sectional area and surface area of the particles, respectively, which both increase with increasing particle loading and decreasing diameter. The gas-phase temperature on the jet centreline was also found to increase approximately linearly with axial distance from the downstream edge of the heating zone to the edge of the measurement region. This indicates near-constant convective heat transfer between the particles and gas throughout this region. This is consistent with the analytical model, which shows that the increase in particle temperature is an order of magnitude greater than that of the surrounding gas.

The temperature rise of the gas-phase downstream from the heating region was found to be proportional to the power absorbed by particles, for a series of particle volumetric loadings and heating powers. However, the magnitude of the gas temperature rise, relative to the absorbed power, was found to increase significantly with a decrease in particle diameter. This indicates that the proportion of the total absorbed radiative heat that is transferred to the gas-phase through convection is strongly dependent on the particle diameter, but not on the particle loading or heating power.

The radial profile of temperature was found to peak at, or near to, the jet centreline, consistent with the time-averaged particle volumetric loading being greatest there. However, the temperature profile was found to be close to uniform within the central jet region of  $|r/D| < 0.5$  for the cases of comparatively low particle number density, with  $\bar{d}_p = 406 \mu\text{m}$  and  $\bar{\phi} \leq 1 \times 10^{-3}$ . In addition, measurements of the temperature on the heating laser up-beam side of the flow ( $r/D > 0$ ) were found to be up to  $10^\circ\text{C}$  greater than that on the down-beam side ( $r/D < 0$ ), consistent with the effect of radiation attenuation. This was especially significant for the flows with  $\bar{\phi} \geq 1 \times 10^{-3}$  and  $\bar{d}_p \leq 238 \mu\text{m}$ .

The measured transmission of the heating beam through the flow was broadly consistent with, although somewhat lower than, that predicted using the particle distribution model, with the relative difference between the measured and predicted attenuations found to increase with  $\phi$ . These differences are consistent with a combination of the slight non-sphericity of the particles that was not accounted for in the model, and/or with a possible role of particle breakage and abrasion in the feeding system leading to the actual particle diameter distribution in the flow differing from that measured beforehand.

The measured axial gradient of the gas-phase temperature on the jet centreline was found to match the values calculated using the simplified one-dimensional model to within 20% for cases with a gradient greater than  $500^\circ\text{C/m}$ . The magnitude of this difference is consistent with imperfect knowledge of the parameters used in the model, in particular the velocities of the gas and particles, radiation attenuation and particle clustering effects. Nevertheless, the general trends between the model and the experiment are consistent. The quantitative agreement is sufficient to confirm that the rate of radiant heating on the particles under the present conditions is some two orders of magnitude greater than that of convective cooling, while the radiative cooling of the particles is an order of magnitude lower again. Hence, the particle cooling processes are dominated by convection, which is coupled with both the particle-fluid transport and buoyancy induced effects. This, in turn, confirms the ongoing need for the further development and application of both new spatially resolved measurements of multiple flow parameters and of new numerical modelling methods to advance quantitative predictive capability.

## References

- Alwahabi, Z. T., K. C. Y. Kueh, G. J. Nathan and S. Cannon (2016). “Novel solid-state solar thermal simulator supplying 30,000 suns by a fibre optical probe”. In: *Optics Express* 24.22, A1444–A1453.
- Balachandar, S. and J. Eaton (2010). “Turbulent Dispersed Multiphase Flow”. In: *Annual Review of Fluid Mechanics* 42, pp. 111–133.
- Banko, A. J., L. Villafañe, J. H. Kim and J. K. Eaton (2020). “Temperature statistics in a radiatively heated particle-laden turbulent square duct flow”. In: *International Journal of Heat and Fluid Flow* 84, p. 108618.
- Chen, H., Y. Chen, H.-T. Hsieh and N. Siegel (2006). “Computational Fluid Dynamics Modeling of Gas-Particle Flow Within a Solid-Particle Solar Receiver”. In: *Journal of Solar Energy Engineering* 129.2, pp. 160–170.
- Davis, D., F. Muller, W. Saw, A. Steinfeld and G. Nathan (2017). “Solar-driven alumina calcination for CO<sub>2</sub> mitigation and improved product quality”. In: *Green Chem.* 19.13, pp. 2992–3005.
- Energy Transitions Commission (2020). *Making Mission Possible - Delivering a Net-Zero Economy*. Report 1.0. Energy Transitions Commission.
- Faust, S., M. Goschütz, S. A. Kaiser, T. Dreier and C. Schulz (2014). “A comparison of selected organic tracers for quantitative scalar imaging in the gas phase via laser-induced fluorescence”. In: *Applied Physics B* 117.1, pp. 183–194.
- Fish, W. M. (2016). “Alumina calcination in the fluid-flash calciner”. In: *Essential Readings in Light Metals*. Vol. 1. Switzerland: Springer International Publishers, pp. 648–652.
- Frankel, A., H. Pouransari, F. Coletti and A. Mani (2016). “Settling of heated particles in homogeneous turbulence”. In: *Journal of Fluid Mechanics* 792, pp. 869–893.
- Gillandt, I., U. Fritsching and K. Bauckhage (2001). “Measurement of phase interaction in dispersed gas/particle two-phase flow”. In: *International Journal of Multiphase Flow* 27.8, pp. 1313–1332.
- Ho, C. K. (2016). “A review of high-temperature particle receivers for concentrating solar power”. In: *Special Issue: Solar Energy Research Institute for India and the United States (SERIIUS) – Concentrated Solar Power* 109, pp. 958–969.
- Incorpera, F., D. Dewitt, T. Bergman and A. Lavine (2007). *Fundamentals of heat and mass transfer*. 6th ed. Wiley.
- Jainski, C., L. Lu, V. Sick and A. Dreizler (2014). “Laser imaging investigation of transient heat transfer processes in turbulent nitrogen jets impinging on a heated wall”. In: *International Journal of Heat and Mass Transfer* 74.Supplement C, pp. 101–112.

- Koban, W., J. D. Koch, R. K. Hanson and C. Schulz (2005). “Oxygen quenching of toluene fluorescence at elevated temperatures”. In: *Applied Physics B* 80.6, pp. 777–784.
- Koban, W., J. D. Koch, R. K. Hanson and C. Schulz (2004). “Absorption and fluorescence of toluene vapor at elevated temperatures”. In: *Physical Chemistry Chemical Physics* 6.11, pp. 2940–2945.
- Kueh, K. C. Y., T. C. W. Lau, G. J. Nathan and Z. T. Alwahabi (2017). “Single-shot planar temperature imaging of radiatively heated fluidized particles”. In: *Optics Express* 25.23, pp. 28764–28775.
- Kueh, K. C. Y., T. C. W. Lau, G. J. Nathan and Z. T. Alwahabi (2018). “Non-intrusive temperature measurement of particles in a fluidised bed heated by well-characterised radiation”. In: *International Journal of Multiphase Flow* 100, pp. 186–195.
- Kumar, A., J.-S. Kim and W. Lipiński (2018). “Radiation Absorption in a Particle Curtain Exposed to Direct High-Flux Solar Irradiation”. In: *Journal of Solar Energy Engineering* 140.6.
- Lau, T. C. W., J. H. Frank and G. J. Nathan (2019). “Resolving the three-dimensional structure of particles that are aerodynamically clustered by a turbulent flow”. In: *Physics of Fluids* 31.7, p. 071702.
- Lau, T. C. W. and G. J. Nathan (2014). “Influence of Stokes number on the velocity and concentration distributions in particle-laden jets”. In: *Journal of Fluid Mechanics* 757, pp. 432–457.
- Lau, T. C. W. and G. J. Nathan (2016). “The effect of Stokes number on particle velocity and concentration distributions in a well-characterised, turbulent, co-flowing two-phase jet”. In: *Journal of Fluid Mechanics* 809, pp. 72–110.
- Lewis, E. W., T. C. W. Lau, Z. Sun, Z. T. Alwahabi and G. J. Nathan (2020). “Luminescence interference to two-colour toluene laser-induced fluorescence thermometry in a particle-laden flow”. In: *Experiments in Fluids* 61.4, p. 101.
- Lewis, E. W., T. C. W. Lau, Z. Sun, Z. T. Alwahabi and G. J. Nathan (2021). “Insights from a new method providing single-shot, planar measurement of gas-phase temperature in particle-laden flows under high-flux radiation”. In: *Experiments in Fluids* 62.4, p. 80.
- Longmire, E. K. and J. K. Eaton (1992). “Structure of a particle-laden round jet”. In: *Journal of Fluid Mechanics* 236, pp. 217–257.
- Luong, M., W. Koban and C. Schulz (2006). “Novel strategies for imaging temperature distribution using Toluene LIF”. In: *Journal of Physics: Conference Series* 45.1, p. 133.

- Meier, A., E. Bonaldi, G. M. Cella, W. Lipinski and D. Wuillemin (2006). "Solar chemical reactor technology for industrial production of lime". In: *Solar Energy* 80.10, pp. 1355–1362.
- Miller, F. and R. Koenigsdorff (1991). "Theoretical analysis of a high-temperature small-particle solar receiver". In: *Solar Energy Materials* 24.1, pp. 210–221.
- Modarress, D., H. Tan and S. Elghobashi (1984). "Two-component LDA measurement in a two-phase turbulent jet". In: *AIAA Journal* 22.5, pp. 624–630.
- Oates, J. A. H. (1998). *Lime and limestone : chemistry and technology, production and uses*. Weinheim, Germany: Wiley-Vch.
- Pouransari, H. and A. Mani (2016). "Effects of Preferential Concentration on Heat Transfer in Particle-Based Solar Receivers". In: *Journal of Solar Energy Engineering* 139.2, pp. 021008–021008–11.
- Siegel, N., M. Gross, C. Ho, T. Phan and J. Yuan (2014). "Physical Properties of Solid Particle Thermal Energy Storage Media for Concentrating Solar Power Applications". In: *Energy Procedia* 49, pp. 1015–1023.
- Siegel, N., M. Gross and R. Coury (2015). "The Development of Direct Absorption and Storage Media for Falling Particle Solar Central Receivers". In: *Journal of Solar Energy Engineering* 137, p. 041003.
- Siegel, N., C. Ho, S. S. Khalsa and G. Kolb (2010). "Development and Evaluation of a Prototype Solid Particle Receiver: On-Sun Testing and Model Validation". In: *Journal Of Solar Energy Engineering-Transactions Of The Asme* 132.2.
- Steinfeld, A., A. Imhof and D. Mischler (1992). "Experimental Investigation of an Atmospheric-Open Cyclone Solar Reactor for Solid-Gas Thermochemical Reactions". In: *Journal of Solar Energy Engineering* 114.3, pp. 171–174.
- Tea, G., G. Bruneaux, J. T. Kashdan and C. Schulz (2011). "Unburned gas temperature measurements in a surrogate Diesel jet via two-color toluene-LIF imaging". In: *Proceedings of the Combustion Institute* 33.1, pp. 783–790.
- Zamansky, R., F. Coletti, M. Massot and A. Mani (2014). "Radiation induces turbulence in particle-laden fluids". In: *Physics of Fluids* 26.7, p. 071701.